The attenuation surface for contrast sensitivity has the form of a witch's hat within the central visual field

Alex S. Baldwin School of Life & Health Sciences, Aston University, Birmingham, UK

Tim S. Meese School of Life & Health Sciences, Aston University, Birmingham, UK

Daniel H. Baker School of Life & Health Sciences, Aston University, Birmingham, UK

Over the full visual field, contrast sensitivity is fairly well described by a linear decline in log sensitivity as a function of eccentricity (expressed in grating cycles). However, many psychophysical studies of spatial visual function concentrate on the central ±4.5 deg (or so) of the visual field. As the details of the variation in sensitivity have not been well documented in this region we did so for small patches of target contrast at several spatial frequencies (0.7–4 c/deg), meridians (horizontal, vertical, and oblique), orientations (horizontal, vertical, and oblique), and eccentricities (0–18 cycles). To reduce the potential effects of stimulus uncertainty, circular markers surrounded the targets. Our analysis shows that the decline in binocular log sensitivity within the central visual field is bilinear: The initial decline is steep, whereas the later decline is shallow and much closer to the classical results. The bilinear decline was approximately symmetrical in the horizontal meridian and declined most steeply in the superior visual field. Further analyses showed our results to be scale-invariant and that this property could not be predicted from cone densities. We used the results from the cardinal meridians to radially interpolate an attenuation surface with the shape of a witch's hat that provided good predictions for the results from the oblique meridians. The witch's hat provides a convenient starting point from which to build models of contrast sensitivity, including those designed to investigate signal summation and neuronal convergence of the image contrast signal. Finally, we provide Matlab code for constructing the witch's hat.

Keywords: visual field, spatial vision, contrast, area summation, inhomogeneity

Citation: Baldwin, A. S., Meese, T. S., & Baker, D. H. (2012). The attenuation surface for contrast sensitivity has the form of a witch's hat within the central visual field. *Journal of Vision*, *12*(11):23, 1–17, http://www.journalofvision.org/content/12/11/23, doi:10.1167/12.11.23.

Introduction

Inhomogeneity of contrast sensitivity

The inhomogeneity of the neural architecture of the human retina (Perry & Cowey, 1985; Curcio & Allen, 1990) and the subsequent neural magnification factors (Daniel & Whitteridge, 1961; Rovamo & Virsu, 1979; Virsu & Rovamo, 1979) lead to nonuniform sensitivity across the visual field (see Strasburger, Rentschler, & Jüttner, 2011 for a review). A detailed understanding of this variation is required to inform the design and interpretation of studies involving spatially extensive stimuli, such as those that investigate area summation of contrast (e.g., Robson & Graham, 1981).

There have been several previous studies of the effect of eccentricity on contrast sensitivity (e.g., Pöppel & Harvey, 1973; Hilz & Cavonius, 1974; Koenderink, Bouman, Bueno de Mesquita, & Slappendel, 1978a, 1978b, 1978c, 1978d; Rovamo, Virsu, & Näsänen, 1978; Rovamo & Virsu, 1979; Rijsdijk, Kroon, & van der Wildt, 1980; Robson & Graham, 1981; Wright & Johnston, 1983; Kelly, 1984; Johnston, 1987; Pointer & Hess, 1989; Rovamo, Franssila, & Näsänen, 1992; Foley, Varadharajan, Koh, & Farias, 2007; Hess, Baker, May, & Wang, 2008). The typical finding in these previous studies is a linear decline in log contrast sensitivity as a patch of target grating is shifted further from the fovea. Several of these studies also investigated spatial frequency effects (e.g., Robson & Graham, 1981; Pointer & Hess, 1989) and found that the sensitivity functions were vertical translations of each other when eccentricity was expressed in terms of stimulus carrier cycles (rather than degrees of visual angle). Another established phenomenon is the *horizontal–vertical anisotropy*, where there is a shallower decline in contrast sensitivity along the horizontal meridian compared to

doi: 10.1167/12.11.23 Received February 22, 2012; published October 25, 2012 ISSN 1534-7362

the vertical meridian. In addition, a *vertical-meridian anisotropy* has been identified where sensitivity is greater in the inferior meridian compared to the superior meridian (see Abrams, Nizam, & Carrasco, 2012 for data and a review).

Stimulus orientation effects have also been reported. In the well-known *oblique effect*, diagonally oriented stimuli are less detectable than horizontal or vertical stimuli, though the effect is found only at mid-to-high spatial frequencies (Campbell, Kulikowski, & Levinson, 1966; Berkley, Kitterle, & Watkins, 1975; Heeley & Timney, 1988; Long & Tuck, 1991). In an extension to this, Rovamo, Virsu, Laurinen, and Hyvarinen (1982) measured spatial acuity for various orientations of grating patches placed in the periphery along several different meridians. At an eccentricity of 25 deg, they found that acuity was affected by an interaction between stimulus orientation and the position of the stimulus in the visual field. Acuity was best for radial grating patches whose orientation was aligned with the meridian on which they were placed such that a line drawn from the fixation point to the patch would be parallel with the grating bars. Typically, they were worst for tangential patches whose orientations were at right angles to this. Rovamo et al. (1982) referred to this effect as the "meridional resolution effect." Sasaki et al. (2006) reported a similar effect for contrast sensitivity. In general we shall refer to these as *relative orientation effects*. This suggests that the eccentricity effects for contrast sensitivity described earlier might interact with absolute and/or relative target orientation.

The studies listed above tended to spread their investigations over a wide range of eccentricities. For example, Pointer and Hess (1989) investigated almost the full width of the visual field (±60 deg) and most of the other studies measured to an eccentricity of 20 deg or more (see Table 1 for details). However, many psychophysical investigations of human spatial vision tend only to concentrate on the central visual field of around ±4.5 deg (e.g., Meese & Summers, 2007) or less (e.g., Carney et al., 2000), where vision is most acute and where visual attention is usually directed. Previous studies have typically gathered very sparse data within this range (often having tested at less than four eccentricities within the range of 0 deg–4.5 deg for spatial frequencies of 4 c/deg or less; see Table 1) and several of them also used stimuli that were spatially quite extensive (Robson & Graham, 1981; Wright & Johnston, 1983; Pointer & Hess, 1989; Rovamo et al., 1992; see Table 1). This means that the information that is available within the central visual field is likely to have been blurred by the large footprint of the probe. Furthermore, with the exception of Abrams et al. (2012)—who did not measure eccentricity functions—none of the previous studies listed used a method to indicate the location of the target patch. This means that stimulus uncertainty (Pelli, 1985) or attention (Carrasco, Penpeci-Talgar, & Eckstein, 2000) might have been a complicating factor in those experiments (see also Michel & Geisler, 2011).

Motivation and aims

To provide a more detailed understanding of the functional inhomogeneity across the central visual field (±4.5 deg), we investigated binocular contrast sensitivity for small stimulus patches whose locations were demarcated using medium contrast surrounding rings. To investigate whether the oblique effect, a relative orientation effect, and/or the two different meridional anisotropies (e.g., Abrams et al., 2012) were important within our region of interest, we also performed our experiment at several different meridians and orientations. For generality and to address a specific question that was raised by our results (see later), we also performed the study at several spatial frequencies.

Within our region of interest we found little effect of orientation. More importantly, however, instead of finding the classical linear result, we found that the decline in log contrast sensitivity with eccentricity was well described by a bilinear function, with an initial slope that was steep followed by a much shallower decline. We summarized our results by constructing an attenuation surface with the shape of an elliptical witch's hat that was slightly deformed in the inferior visual field. Although our study shows that the inhomogeneity for contrast sensitivity is a little more complex than previously thought, the witch's hat is straightforward to construct (see Appendix B) and provides a valuable component to the front end of any model of contrast sensitivity, particularly if the stimuli are concentrated in the central visual field.

Methods

Equipment

Three experimental setups were used. In each case, stimuli were stored in a Cambridge Research Systems (CRS) ViSaGe and presented on a gamma-corrected CRT monitor (Nokia Multigraph 445X, Philips MGD403, or Eizo Flexscan T68). All monitors had a refresh rate of 120 Hz, and mean luminances varied from 60 cd/m^2 to 85 cd/m^2 between the monitors. The stimuli had 12 pixels per carrier cycle for spatial frequencies of 2 to 4 c/deg. The viewing distance for the 4 c/deg stimuli was 119 cm. At this distance, 48 pixels on the screen subtended 1 deg of visual arc. The viewing distance was adjusted to scale the retinal image to the desired spatial frequency (59.5–119 cm for the

Publication	Spatial freq. (c/deg)	Stimulus window/type	Size	No. of samples within 4.5 deg	Orientation	Eccentricity		Meridian
						Cycles	Degrees	
Pöppel & Harvey, 1973	N/A	Bright spot	0.08 deg radius	3	N/A		0–80	H
Hilz & Cavonius, 1974	2–45	Circle	2 deg–5 deg	5	Vertical	0–180	0–23	H
Koenderink et al., 1978a	2–25.5	Square	0.5 × 0.5 deg	4	Horizontal	0–80	0–8	H
Rovamo et al., 1978	1–32	Semicircle	1 deg radius	3	Vertical	0–60	0–30	H & V
Rijsdijk et al., 1980	0.35–6	Plaid patch	1 × 1 cycles	4	H × V	0–36	0–6	H, V, & D
Robson & Graham, 1981	1.5–24	Raised-cosine	4 × 4 cycles	3	Horizontal	0–32	0–21	V
Wright & Johnston, 1983	0.25–9	Rectangle	3.5 deg × 0.7 deg	4	Vertical	0–72	0–12	V
Kelly, 1984	0.5–16	Annulus	12–500 deg^2	2	Concentric	0–36	0–12	N/A
Johnston, 1987	2–12	Square	12 × 12 cycles	2	H & V	0–480	0–40	H
Pointer & Hess, 1989	0.05–12.8	Gabor	σ = 3.2 cycles	1	Horizontal	0–96	0–60	H & V
Rovamo et al., 1992	3	Not specified	6 × 6 cycles	2	Vertical	0–39	0–13	H
Foley et al., 2007	4	Gabor	σ = 1 cycle	4	Vertical	0–20	0–5	H
Hess et al., 2008	0.5–3	Gabor	σ = 1 cycle	1	Horizontal	0–30	0–60	H
Present Study	0.7–4	Log-Gabor	sfbw: 1.6 oct. oribw: ±25 deg	9	H, V, & D	0–18	0–26	H, V, & D

Table 1. Experimental details from previous studies on the effect of retinal eccentricity on contrast sensitivity. Where spacings varied across different conditions, we have shown the number of samples within 4.5 degrees for the conditions most similar to ours (i.e., spatial frequency of 4 c/deg). Abbreviations: H = horizontal; V = vertical; D = diagonals; sfbw = spatial frequency bandwidth (full width at half height); oribw = orientation bandwidth (± half width at half height).

range 2–4 c/deg). For stimuli with a spatial frequency below 2 c/deg, the stimulus was first doubled in size on the screen (24 pixels per carrier cycle) and then the viewing distance was adjusted appropriately (41.7–83.3 cm for the range 0.7–1.4 c/deg).

Most of the data collection for ASB and DHB was performed using different experimental setups. To ensure that this was not responsible for the individual differences that we found between these observers (see Results section), ASB and DHB each ran a subset of the conditions from Experiment 1 on each other's equipment. In each case, the details of the results were consistent within observer rather than within laboratory, confirming that the use of different equipment was not important.

Stimuli

The stimuli for this experiment were luminance-modulated Cartesian-separable cosine-phase log-Gabor patches. These were defined in Fourier space by the product of a one-dimensional log-Gaussian in the spatial frequency dimension and a one-dimensional Gaussian in the orthogonal dimension (see appendix C of Meese [2010] for details). Stimulus contrasts are expressed as delta-contrast:

$$c_{delta} = \frac{L_{max} - L_{mean}}{L_{mean}}, \quad (1)$$

which is linearly related to Michelson contrast for the stimuli used here, and also in dB re 1% as follows:

$$c_{dB} = 20\log_{10}(100c_{delta}). \quad (2)$$

Our stimuli had spatial frequencies of 0.7, 1, 1.4, 2, 2.8, and 4 c/deg and a minimum resolution of 12 pixels/cycle. This was sufficient to avoid problems with luminance artifacts that can arise from adjacent pixel nonlinearity (García-Pérez & Peli, 2001). The stimuli had spatial frequency bandwidths of 1.6 octaves (full-width at half-height) and orientation bandwidths of ±25° (±half-widths at half-height), which is a good approximation of individual receptive field properties in early vision (Meese, 2010). They had orientations of 90° (horizontal), 135° (left oblique), 45° (right oblique), and 0° (vertical), as shown in Figure 1. The stimulus duration was 100 ms.

To reduce extrinsic uncertainty a circular ring (diameter of three carrier cycles, line width of 1 pixel, contrast set to 25%) was placed around the target location and was visible continually. An identical ring was also used to aid central fixation such that in most conditions, two rings were visible. The one exception was when the target was placed in the center of the visual field, where only a single central ring was needed. In Experiment 2, the rings were replaced with pairs of dots as described in the results section for that experiment.

Observers

There were four observers. ASB, DHB, and TSM are the authors and SAW was another experienced observer. The observers were 22, 28, 46, and 44 years old, respectively. Observers wore optical correction

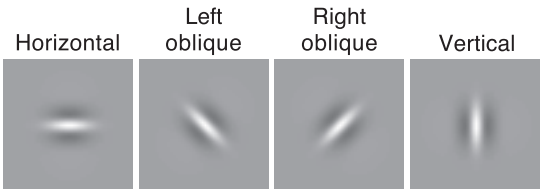

Figure 1. Examples of the cosine-phase Cartesian-separable log-Gabor stimuli used in the experiments.

appropriate for the viewing distances tested when required. All experiments were performed binocularly with natural pupils.

Procedures

In Experiment 1, 4 c/deg log-Gabor stimuli of all four orientations were presented at four eccentricities (0, 6, 12, and 18 cycles; equivalent to 0 deg, 1.5 deg, 3 deg, and 4.5 deg of visual angle) along eight hemi-meridians (0°, 45°, 90°, 135°, 180°, 225°, 270°, and 315°) radiating from the center of the visual field. This is equivalent to four meridians using the +ve and −ve sign convention in Figure 2. Stimuli were blocked such that in each session, thresholds were determined for a single stimulus orientation at a single position in the visual field (i.e., there should be no extrinsic uncertainty about the stimulus properties). There were 100 blocks (the 25 locations in Figure 3 × 4 patch orientations) that were repeated in a randomized order four times by two observers (ASB and DHB). Two more observers (SAW and TSM) performed a subset of the conditions.

Thresholds were measured using a two-interval forced-choice (2IFC) procedure where each trial contained two temporal intervals, each marked by a beep. In one randomly chosen interval the stimulus was presented at a contrast selected by a three-down, one-up staircase procedure. The other interval was blank (i.e., it was held at mean luminance). The observer's response was made by pressing one of two buttons to indicate which interval they thought contained the target. Feedback on correctness of response was provided by the pitch of an additional beep after the response. Each condition was repeated four times by each observer and the thresholds (calculated using a probit fit to the staircase data) were then averaged.

The conventional procedure for measuring contrast sensitivity at various eccentricities is to vary the position of the fixation mark while keeping the target patch in the center of the display. This design ensures that the results are not affected by any spatial inhomogeneities in the equipment, such as variation of mean luminance across the display (García-Pérez & Peli, 2001). However, our prime motivation for carrying out this study was to estimate the spatial inhomogeneity of sensitivity across a display field so

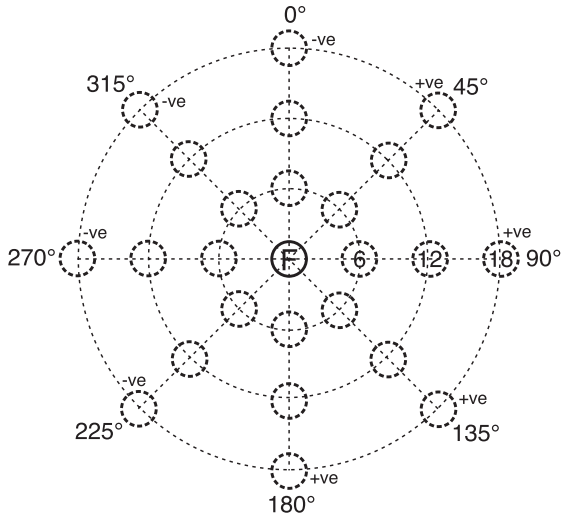

Figure 2. Spatial layout of the main stimulus position used in Experiment 1. Note the four meridians (vertical, horizontal, left oblique, and right oblique) and the four eccentricities (0, 6, 12, and 18), expressed in carrier cycles. Finer sampling was used in Experiment 2 and Experiment 3. The letter F labels the central fixation circle and was not present in the experiment. The +ve and -ve labels signify our sign convention used with the four meridians. Alternatively, we sometimes find it convenient to refer to the directions of the eight hemi-meridians as they are labeled around the perimeter of the figure.

that this could be used in subsequent models of area summation of contrast (e.g., see Baker & Meese, 2011; Meese & Summers, 2012). For this reason, the fixation ring was always presented in the center of the display and the target positions were varied across the display. A control experiment using the conventional method and a subset of the conditions from Experiment 1 confirmed that that our principal findings (e.g., bilinearity) were the same using either method.

The methods for our other experiments were similar to those used for Experiment 1, with detailed differences described in the relevant part of the Results section.

Results

Experiment 1: Sensitivity across the central visual field for four meridians and four stimulus orientations

Contrast sensitivity along each of the eight hemi-meridians is shown in Figure 3 for two observers. The rates of decline as determined by linear regression are shown in Table 2. Consistent with previous results (e.g., Pointer & Hess, 1989), sensitivity was greatest at the center of the visual field, and the decline in sensitivity was steeper along the vertical meridian than along the

horizontal meridian. The diagonal meridians appear to show a decline in sensitivity that is intermediate between those for the horizontal and vertical meridians.

The main effect of eccentricity was confirmed by statistical analyses (not shown), but our deeper interest involved the factor of orientation. A pair of three-way repeated-measures analysis of variance (ANOVA) tests was performed using predictive analytics software (PASW Statistics; version 18.0, IBM Corp.) for each observer. (Results from Mauchly's test of sphericity are also given. In all cases we found no significant violation of sphericity and therefore no correction of the ANOVA was necessary.) One of the tests was for factors of eccentricity, hemi-meridian, and absolute patch orientation. The other test was the same, except that patch orientation was defined relative to the meridian that the stimulus was placed on. For example, a right oblique patch placed on the 225° to 45° meridian (see Figure 3) would have an absolute orientation of 45°, but a relative orientation of 0°. These analyses were designed to test for the oblique effect and a relative orientation effect, respectively.

Absolute orientation effects

Effects of absolute patch orientation were found for both ASB (Mauchly's test n.s. $\chi^2(5) = 5.45$, $p = 0.43$; ANOVA $F(3, 9) = 11.50$, $p < 0.01$) and DHB (Mauchly's test n.s. $\chi^2(5) = 4.01$, $p = 0.61$; ANOVA $F(3, 9) = 5.52$, $p = 0.02$), but were small and not consistent across observers. ASB was most sensitive to vertical patches and least sensitive to horizontal patches (compare blue and red symbols in the top four panels of Figure 3), whereas DHB was most sensitive to horizontal patches and least sensitive to left-oblique patches (compare red and magenta symbols in the lower four panels of Figure 3).

We performed three paired Bonferroni-corrected t tests per observer to further investigate the orientation effects. In the first analysis, two t tests compared each patch orientation with its orthogonal patch orientation (i.e., horizontal vs. vertical, left oblique vs. right oblique) pairing by location in the visual field (meridian and eccentricity). In a second analysis we averaged the results across (a) the vertical and horizontal stimulus orientations and (b) the two oblique stimulus orientations and compared these two sets of results to test for an overall oblique effect. ASB showed significant differences in sensitivity between the horizontal and vertical stimuli and between the two oblique orientations ($p < 0.01$ in each case); however a small overall oblique effect that was found in the second analysis (0.13 dB) was not significant ($p = 0.23$). For DHB there was no difference between either the horizontal and vertical conditions ($p = 0.24$) or the two oblique conditions ($p = 0.09$). The overall oblique effect was significant for DHB ($p < 0.01$) but small in size (0.66 dB). This effect is smaller than those found at higher

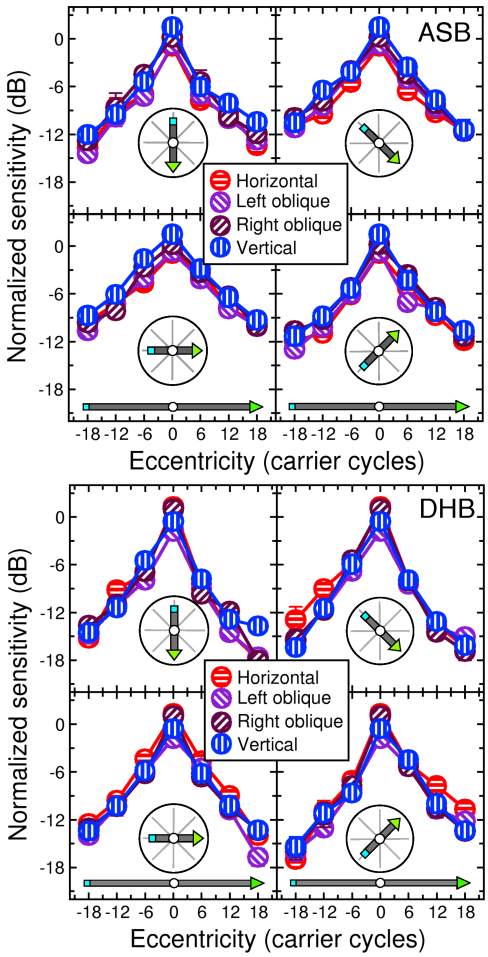

Figure 3. Contrast sensitivity from Experiment 1 for ASB (top) and DHB (bottom). Different plots are for the four different meridians, as shown by the insets. Within each plot the different symbols are for the four different stimulus orientations. The spatial frequency was 4 c/deg. Error bars in this and all other figures show ±1 *SE* where larger than symbol size. For clarity, the results are normalized to the sensitivity of the central vertical patch for each observer.

spatial frequencies (e.g., Campbell et al., 1966 found effects in the order of 2–6 dB for spatial frequencies in the range of 10–30 c/deg), though it is well known that the oblique effect diminishes at lower spatial frequencies (Campbell et al., 1966; Long & Tuck, 1991) to levels around those found here, or a little above. Overall, we conclude that for the stimulus conditions here the absolute orientation effects were of little concern, since when they were statistically significant they were inconsistent across observers and were small in size.

Relative orientation effects

Comparing the mean contrast detection threshold of patches aligned with the meridian they were placed on with that of patches having the orthogonal orientation, we found a small radial advantage for

	Individual hemi-meridian fall-off fits (dB/cycle)								Averaged fits for meridians (dB/cycle)		
Observer	0°	45°	90°	135°	180°	225°	270°	315°	Vertical	Horizontal	Diagonal
ASB	0.72	0.61	0.55	0.64	0.65	0.65	0.55	0.59	0.69 ± 0.04	0.55 ± 0.00	0.62 ± 0.01
DHB	0.79	0.70	0.79	0.90	0.92	0.86	0.74	0.84	0.86 ± 0.07	0.77 ± 0.03	0.83 ± 0.04

Table 2. Gradient of decline in log contrast sensitivity (in dB/cycle) for linear fits to the data from Experiment 1. Averages are given as the mean ±1 standard error.

both ASB (0.25 dB) and DHB (0.56 dB). The ANOVA that tested relative orientation (across all four orientations) found this effect to be nonsignificant for ASB (Mauchly's test n.s. $\chi^2(5) = 4.39$, $p = 0.56$; ANOVA $F(3, 9) = 1.54$, $p = 0.27$), but significant for DHB (Mauchly's test n.s. $\chi^2(5) = 0.44$, $p > 0.99$; ANOVA $F(3, 9) = 4.07$, $p = 0.04$). However, despite the result for DHB there were no significant pairwise comparisons across aligned and orthogonal patches.

Previous studies that have reported an effect of relative orientation (Rovamo et al., 1982; Sasaki et al., 2006) have performed the experiment at greater eccentricities (25 deg and 15.5 deg, respectively), so it is possible that relative orientation effects are restricted to the more eccentric locations. To test this possibility, we looked for, but did not find, a two-way interaction between eccentricity (ASB: Mauchly's test n.s. $\chi^2(2) = 0.74$, $p = 0.69$; DHB: Mauchly's test n.s. $\chi^2(2) = 3.30$, $p = 0.19$) and relative orientation (ASB: ANOVA $F(6, 18) = 0.59$, $p = 0.74$; DHB: ANOVA $F(6, 18) = 2.09$, $p = 0.11$). However, the results of a supplementary experiment (not shown) confirmed that when we approximated the conditions of Sasaki et al. (2006) by using larger stimuli (we halved our initial bandwidths) at a greater eccentricity (62 cycles at 4 c/deg) we did find a relative orientation effect. Thus, while we can confirm the existence of this effect, we also conclude that it is not sufficiently large or consistent to be relevant to the central visual field, for studies of this type at least.

Results for vertical stimuli

As there was very little effect of target orientation, our other two observers (SAW & TSM) performed the experiment for vertical stimulus patches and the vertical and horizontal meridians only. Their results are shown in Figure 4 along with the corresponding results for ASB and DHB, replotted from Figure 3. Overall, the decline in sensitivity with eccentricity was slightly steeper than that found in previous studies. For example, Pointer and Hess (1989) found declines of 0.5 and 0.33 dB/cycle for the vertical and horizontal meridians, respectively. These are shown by the dashed lines in Figure 4, against which our results can be seen to decline more rapidly.

Casual inspection of Figures 3 and 4 suggests that the decline in log contrast sensitivity with eccentricity is not linear. For most observers and hemi-meridians there was a steep initial decline followed by a shallower decline. However, the sampling of eccentricity in this experiment was not sufficiently fine to identify the location of the transition between the two slopes (the knee point, see below) with much precision. Therefore, we repeated some of the conditions from Experiment 1 using a finer sampling regime.

Experiment 2: Identifying the location of the knee point using finely-spaced targets

Experiment 2 was similar to Experiment 1, but only the vertical and horizontal meridians were tested and the target orientation was always vertical. The experiment was performed by all four observers. Retinal eccentricity was sampled more finely than in Experiment 1, spanning 0–9 cycles in intervals of 1.5 cycles. However, a problem with the fine spacing in this experiment was that it would have caused an overlap between the ring that was used to aid fixation and that which was used identify the target location. To avoid this problem each ring was replaced by a pair of dots, such that the target was flanked by one pair of dots and the central fixation point was flanked by another pair of dots. The pair of dots was oriented either horizontally or vertically when testing the vertical or horizontal meridians, respectively.

The results from Experiment 2 are shown in Figure 5, averaged across all four observers. A comparison of the data points against the extrapolated gradient of the initial decline (the dotted line) emphasizes the nonlinear character of the function. Although the knee point did not fall within the range of the fine sampling results (triangles), taken together with the results from Experiment 1 (circles, averaged from the same four observers for the same stimulus configurations) they suggest that the knee point is placed at about nine cycles. This is addressed more thoroughly by our detailed account of the curve fitting in a later section.

Experiment 3: Does the knee point depend on stimulus cycles or visual angle?

In Experiments 1 and 2, only a single spatial frequency was used and so it did not matter whether the eccentricity axis was plotted in terms of stimulus cycles or visual

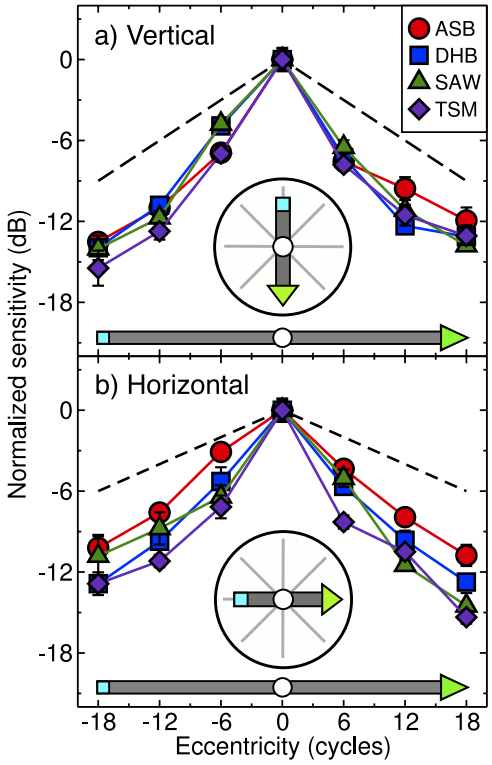

Figure 4. Contrast sensitivity across the vertical (top) and horizontal (bottom) meridians for each of the four observers. The stimuli were vertical log-Gabor patches with a spatial frequency of 4 c/deg (Experiment 1). The eccentricity is expressed in stimulus carrier cycles, the visual angle of the range shown here is –4.5 deg to +4.5 deg. The black dashed lines are for comparison and indicate the overall decline in sensitivity with eccentricity for the vertical (0.5 dB/cycle) and horizontal (0.33 dB/cycle) meridians estimated by Pointer and Hess (1989). These were derived from a much greater range of eccentricities (0–96 cycles) than those investigated here. The initial decline in sensitivity measured here is steeper than that found by Pointer and Hess (1989) but at greater eccentricities the two studies become more similar.

angle. However, we wondered which one of these, if either, the knee point depends on. For example, if it were determined by retinal anatomy such as cone density (Curcio, Sloan, Kalina, & Hendrickson, 1990; see Appendix A) we might expect degrees of visual angle to be the determinant, whereas if spatial frequency dependent cortical processes are involved then eccentricity as measured in stimulus cycles might be the critical factor. Experiment 3 was based on a subset of the conditions from Experiment 1, using horizontal log-Gabors placed along the 180° (inferior) hemi-meridian. The sampling of the hemi-meridian was twice that used in Experiment 1 (i.e., from 0–18 cycles in intervals of three cycles). The experiment was conducted using six spatial frequencies (0.7, 1, 1.4, 2, 2.8, and 4 c/deg).

Results are shown in Figure 6 (the same data are shown in the two columns but plotted against different

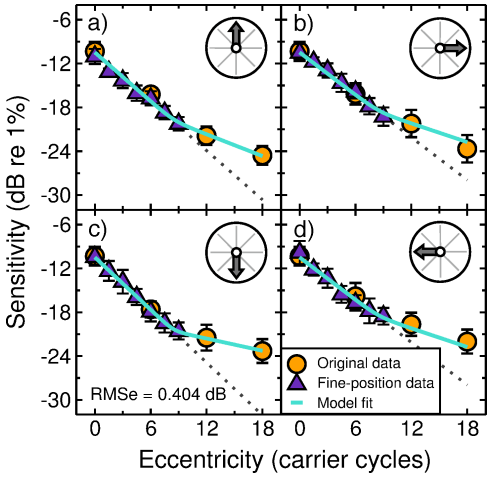

Figure 5. Contrast sensitivity from Experiment 2 using the fine-positioning regimen. Results are averaged across four observers (ASB, DHB, SAW, and TSM). The triangles are for this experiment and the circles are for the same four observers for the vertical patches from Experiment 1. The curve-fitting is explained in the Descriptive modeling section below. It is an eight-parameter fit across the four panels (see forward to Table 4 for the parameter values for fits to the results for individual observers and the averaged results shown here). The overall RMS error for this fit is 0.404 dB. The dotted lines extrapolate the initial (m_1) gradient (see Descriptive modeling section).

x-axes). As expected, contrast sensitivity decreased with increasing spatial frequency. In agreement with previous studies (Robson & Graham, 1981; Pointer & Hess, 1989), the functions for each spatial frequency are approximately parallel when eccentricity is expressed in carrier cycles (left column) but the family of curves splays outwards when the same results are plotted as functions of visual angle (right column). This confirms previous conclusions that the overall rate of decline in contrast sensitivity with eccentricity depends on the distance from the central fovea expressed in number of stimulus cycles. However, our main aim here was to establish whether this was also the case for the knee point. Casual inspection of Figure 6 suggests that it is. We consider this more closely in the following modeling section.

Descriptive modeling

Bilinear model equations

We fitted descriptive model curves to our data for two reasons. First, we wanted to produce convenient quantitative summaries of our results. Second, we wanted to determine whether our casual analyses of the results were correct. For example, were we justified in

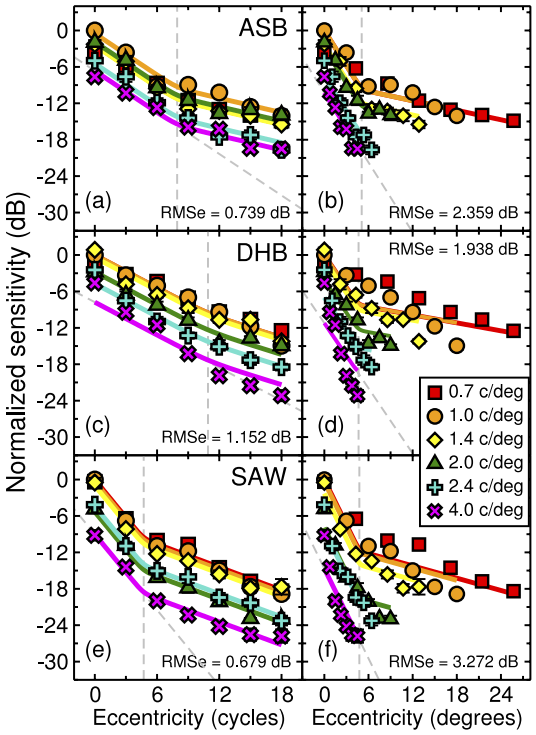

Figure 6. Contrast sensitivity from Experiment 3 for six spatial frequencies (different symbols). Different rows are for different observers (ASB, DHB, and SAW). The same results are shown against eccentricity in cycles of the stimulus carrier frequency (a, c, and e) and degrees of visual angle (b, d, and f). The solid curves are the fits of bilinear functions, with different fitting methods for the two columns (see modeling section). Parameter values for the fits are shown in Table 3. Grey dashed lines show the positions of the knee points (v) and the m_1 gradient parameters (see Descriptive modeling section).

claiming that the initial decline in contrast sensitivity with eccentricity is steeper than the subsequent decline?

We devised an equation that produced a bilinear curve as follows:

$$S = -\log_{10}\left(\frac{10^{m_1 E}}{10^{(m_1-m_2)v} + 10^{(m_1-m_2)E}}\right) + K, \quad (3)$$

where S is contrast sensitivity (expressed in dB) and E is eccentricity expressed in either degrees of visual angle or in stimulus carrier cycles (e.g., compare the two columns in Figure 6). The free parameters are m_1 and m_2, which control the slopes of the first and second limbs of the function, respectively (they are the gradients of negative slopes in dB/cycle), v, which controls the location of the knee point (in the units of eccentricity), and K, which controls the vertical position of the function. To impose a convenient meaning on K, we set $K = k_1 + k_2$, where k_1 is given by:

$$k_1 = \log_{10}\left(\frac{1}{10^{(m_1-m_2)v} + 1}\right). \quad (4)$$

With this arrangement, the degree of freedom transfers from K to k_2, which is expressed in dB re 1% as defined above (Equation 2). It is the observer's contrast sensitivity to a stimulus presented in the center of the fovea (i.e., the vertical dB offset of the eccentricity function from 0 dB).

Equations 3 and 4 do not allow a fit where the initial slope is shallower than the subsequent slope. A peculiar property of this equation is that if m_1 is set lower than m_2 then their meaning switches (i.e., m_2 describes the initial slope and m_1 describes the subsequent slope). As this would cause problems in the fitting, the parameters were constrained such that $m_1 \geq m_2$.

A bilinear function that flexes in the opposite direction, where the first limb is shallower than the second, is produced by adjusting Equations 3 and 4 to produce Equations 5 and 6 as follows:

$$S = \log_{10}\left(\frac{10^{-m_1 E}}{10^{(m_1-m_2)v} + 10^{(m_1-m_2)E}}\right) + K \quad (5)$$

and

$$k_1 = -\log_{10}\left(\frac{1}{10^{-(m_1-m_2)v} + 1}\right). \quad (6)$$

For these equations parameters were constrained such that $m_1 \leq m_2$. Because of the shapes that these functions produce when plotted as radial functions in 3D (we explain this more fully in the Discussion), we refer to Equation 3 as the witch's hat and Equation 5 as the samurai hat. To reiterate, for each hat, m_1 and m_2 describe the absolute gradients of the first and second limb of a bilinear function. For the witch's hat, m_1 is greater than or equal to m_2, whereas for the samurai hat, m_1 is less than or equal to m_2.

Which hat fits best? The witch hat fits best

The fitting of Equations 3 and 5 was done using fminsearch in Matlab, which minimized the root mean square (RMS) error of the fit (in dB) using a simplex algorithm.

Our initial aim was to determine whether a bilinear description of our results is justified over a linear description. We did this by comparing the RMS errors of the fits by the two different hat functions to the results from each hemi-meridian that we measured. Each hemi-meridian was fitted independently with four free parameters: m_1, m_2, v, and k_2. If a linear decline in sensitivity was more appropriate on average, then neither hat should win out over the other. The results of this analysis applied to each of the three main experiments and the two control experiments described in the Methods section (the more traditional *target central on monitor* presentation paradigm and the

equipment swap control) are shown in Figure 7. In the great majority of cases (71 out of 76) the RMS error for the witch's hat was lower than for the samurai hat. A sign test showed that this difference was highly significant for each of the three main experiments ($p < 0.001$). For both control experiments the witch's hat always outperformed the samurai hat; this was statistically significant where sufficient data had been gathered for it to be so ($p = 0.031$ for the fixation control, $p = 0.125$ for the equipment control).

How many parameters do we need?

In general, our model (Equation 3) was designed to fit the results from individual hemi-meridians, which involves four free parameters. As the overall sensitivity parameter (k_2) should be common to all meridians, it follows that the number of free parameters needed to fit a family of n hemi-meridians is $1 + 3n$. However, by yoking other parameters across different meridians it is possible to reduce the number of free parameters while maintaining a good fit to the data. We were interested in how far this could be taken because reducing the number of parameters might allow an estimate to be made of an entire witch's hat from a smaller dataset. For example, we wondered whether we could justify collapsing across the left and right sides of the horizontal meridian (for the binocular stimulus presentation used here).

Akaike's information criterion (AIC; Akaike, 1974; see also Peirce, 2007) was used to evaluate the benefit of the free parameters in several variants of the model by playing off the number of free parameters against the RMS error of the fit. The AIC value for a model is defined as:

$$AIC = n\log(RMSe) + 2p \quad (7)$$

where n is the number of data points, $RMSe$ is the root mean square error of the model fit to the data, and p is the number of model parameters.

We considered several model variants involving various different symmetries across the visual field. The variants with the fewest and the greatest number of constraints had 13 and four free parameters, respectively. The former was capable of producing the most irregular surface, whereas the latter was rotationally symmetric. The results of fitting these model variants to the data from Experiments 1 and 2 (vertical stimuli placed along four cardinal hemi-meridians) are shown in Table 3. The model variant with the lowest AIC score was the eight-parameter model, which yoked the knee point position for all directions and mirrored the

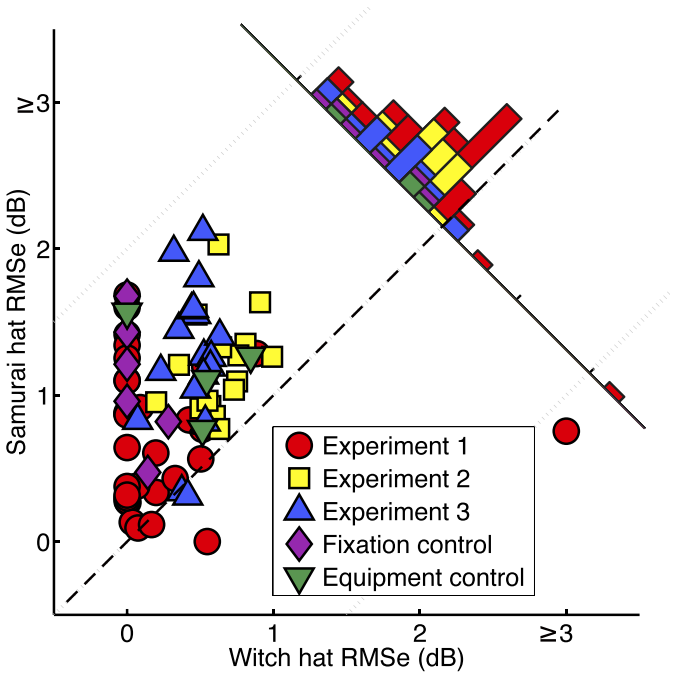

Figure 7. Comparison of the quality of the fits using the witch's hat and the samurai hat functions. RMS errors for the two fitting methods are compared against each other in a scatter plot for the three main experiments and the two control experiments. For convenience of presentation, RMS errors were capped at 3 dB (i.e., points where the RMS error was > 3 dB had this value reset to 3 dB). This was necessary for just a single point. Points on the dashed line $y = x$ indicate results that were equally well fit by a witch's hat or a samurai hat function (usually because they were best fit by a linear function). Above-left of this line, the results were best fit by a witch's hat function, and below-right of this line the results were best fit by a samurai hat function. The histogram in the upper right shows the distribution of the differences between the witch's hat and the samurai hat RMS errors, using the same color-code as in the scatter plot.

Model description	Free parameters	RMS Error (dB)	AIC
Separate m_1, m_2, and v for each direction. Global k_2.	13	0.38	−13.4
Separate m_1, m_2, and v for superior and inferior, combined for horizontals. Global k_2.	10	0.40	−17.7
Combined m_1, m_2, and v for horizontals and for verticals. Global k_2.	7	0.45	−19.0
Global m_1, m_2, v, and k_2.	4	0.69	−7.5
Combined m_1, m_2 for horizontals. Global k_2 and v.	8	0.40	−21.2*

Table 3. Number of parameters, RMS errors, and Akaike's information criterion for fitting the results from the four hemi-meridians in Experiments 1 and 2 (averaged across four observers) with different versions of the bilinear witch's hat model. The model variant in the bottom line is the one fitted to Figure 5.

	Superior		Inferior		Horizontal		Global	
Observer	m_1	m_2	m_1	m_2	m_1	m_2	v	k_2
ASB	1.05	0.40	1.05	0.21	0.76	0.31	8.0	8.6
DHB	1.05	0.56	1.31	0.27	1.00	0.47	8.2	12.6
SAW	1.01	0.49	1.09	0.33	0.92	0.44	10.5	12.2
TSM	1.38	0.49	1.35	0.28	1.22	0.45	7.9	8.5
Average	1.12	0.50	1.20	0.28	0.97	0.43	8.5	10.5

Table 4. Model fit (eight-parameter version, see Table 3) to the data from Experiments 1 and 2 for each observer and to the averaged data of the four observers.

gradients across the horizontal meridian but allowed different gradients for the superior and inferior hemi-meridians. Nested model hypothesis testing also showed this model to provide the best fit when the number of parameters required is taken into account (F-statistic, with significance set at $p = 0.05$). Increasing the number of free parameters from 8 to 13 produced negligible improvement in the RMS error of the fit (compare top and bottom rows in Table 3), providing further confirmation that our choice of the eight-parameter variant is sound.

The witch's hat provides a good fit to our cardinal results

Fits of the eight-parameter model above are shown for the vertical stimulus patches from Experiments 1 and 2 (for which we had data from all four observers) in Figure 5. To reiterate, the offset parameter k_2 and the knee parameter v were each yoked across the four meridians, and m_1 and m_2 were yoked across the two horizontal hemi-meridians. With this simplification, the fitting procedure placed the knee point at 8.5 cycles (see Table 4). Increasing the number of free parameters by two so that v was yoked in the same way as m_1 and m_2, produced no improvement in the quality of the fit and did not change our conclusions about the location of the knee point.

Interpolation between cardinal meridians

We have measured the decline in contrast sensitivity along several hemi-meridians, but how can this information be combined to summarize sensitivity across a two-dimensional retina? One way is to construct an attenuation surface that interpolates radially between the fits to the four cardinal hemi-meridians. Bilinear fits to the results from Experiment 1 collapsed over target orientation (for ASB and DHB) were used to define a witch's hat shaped attenuation surface (Figure 9) by allowing the parameters to vary elliptically with the angle of the hemi-meridian, and where these conic parameters were controlled separately for each quadrant (the details for this are provided in the Matlab code in Appendix B).

To check the success of our approach we compared the sensitivity predicted by the witch's hat derived from the four cardinal hemi-meridians to the data gathered from the four diagonal hemi-meridians. This is to judge how well the solid cyan curves are approximated by the dashed purple curves in Figure 8. For both observers, the RMS errors for these predictions (dashed purple curves, no free parameters) compared well with the general quality of fits that were achieved to the larger data sets in Table 3 (see figure caption for details).

Scale invariance and the location of the knee point

The model fitting to the results in Figure 5 placed the knee point at 8.5 cycles for 4 c/deg stimuli. Here we ask whether this result generalizes across other spatial frequencies, or whether the knee point is better described in terms of a fixed visual angle (e.g., 2.125 deg). To test this we fitted the model to the results from Experiment 3 by yoking all of the parameters for a single hemi-meridian across spatial frequency, with the exception of the overall sensitivity parameter, k_2. For each of the three observers, we tested whether the fit was better when m_1, m_2, and v were yoked in terms of carrier cycles or scaled in terms of degrees of visual angle. Testing every combination created the eight factorial set of model variants in Table 5.

For each of the three observers, the family of spatial frequency functions (Figure 6) were better fit when the three parameters were yoked by cycles than by degrees of visual angle (compare first and last columns in Table 5). A comparison of these two methods of fitting is shown for each observer in the left and right columns of Figure 6. For ASB, SAW, and the average of the three observers, yoking by cycles for all three parameters produced the best fits overall, whereas for DHB, slightly better fits were achieved when the knee parameter was yoked by degrees of visual angle, though this difference was marginal (see the entries marked by asterisks in Table 5).

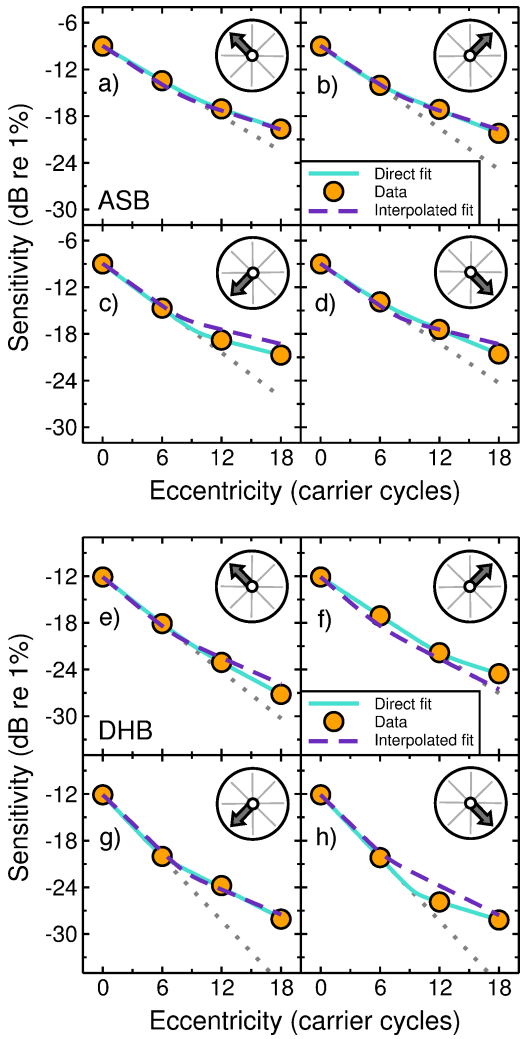

Figure 8. Comparison of the predictions and direct fits to the results for the diagonal meridians. The solid cyan curves are direct fits of the witch's hat to the data involving 13 free parameters (equal to the number of data points). The dashed purple curves are predictions derived by radial interpolation from the cardinal hemi-meridians using the witch's hat (no free parameters). Data points are the thresholds for stimulus patches presented along the diagonal hemi-meridians collapsed across patch orientation. For observer ASB the RMS error for the direct fit was 0.03 dB and the RMS error from the interpolated fit was 0.63 dB. For DHB the RMS errors were 0.09 dB and 0.96 dB, respectively. The dotted grey lines are extrapolations of the m_1 gradient from the direct fit.

The parameters and RMS errors for the scale invariant model fits are shown in Table 6. Note that the sequence of k_2 offsets describes the contrast sensitivity function for the range of spatial frequencies tested.

The average value of the knee parameter (v) was 7.5, which compares favorably with the average value of 8.5 derived from the larger data set in Experiments 1 and 2. However, we did note that the current estimates were more variable across observers than they had been previously (Table 4). Fitting again with the knee position fixed to that reported for each observer in Table 4, we found the same scale invariance for a negligible decline in the RMS errors (not shown).

Discussion

The decline in log contrast sensitivity with eccentricity is not linear

Previous research (Robson & Graham, 1981; Pointer & Hess, 1989; Foley et al., 2007) has reported a linear decline in log contrast sensitivity with eccentricity. However, our detailed investigation of the central 9° of the visual field has shown that the decline is nonlinear and is well described by a bilinear function for stimuli within the 0.7–4 c/deg spatial frequency range. Moreover, the initial decline (1.12 dB/cycle) is much steeper than the classical reports of 0.3–0.5 dB/cycle (Pointer & Hess, 1989) and extends to a radius of around 8.5 cycles (Table 4), though it is difficult to be precise owing to some of the variation that we observed (Table 6). Nevertheless, our results imply that centrally placed target gratings with diameters of this order are subject to much more severe attenuation with eccentricity than has often been supposed. For example, sensitivity to a 4 c/deg patch of grating at an eccentricity of 2.125 deg is only one third of that at its center.

The average value of m_2 for the four cardinal meridians in Table 4 was 0.41 dB/cycle. Thus, the gradients of the second limbs are much closer to the classical result (0.3–0.5 dB/cycle) than are those of the initials limbs. This is probably because previous studies have concentrated on the wider visual field, where the second limb might be expected to dominate the analysis, and have used fairly large stimulus patches, thereby blurring the transition between the two limbs. However, close inspection of some of the results in the extensive Pointer and Hess (1989) study does reveal several instances of the bilinearity that we are advocating (e.g., see their figure 2d).

The decline in contrast sensitivity is scale-invariant within our tested range

Our finding of a decline in contrast sensitivity that is scale-invariant is in agreement with previous psychophysical results (Robson & Graham, 1981; Pointer & Hess, 1989). However, sensitivity functions that are vertical translations of each other when eccentricity is expressed in stimulus carrier cycles do not derive from retinal physiology in a straightforward way. For example, we tested a model that predicted contrast

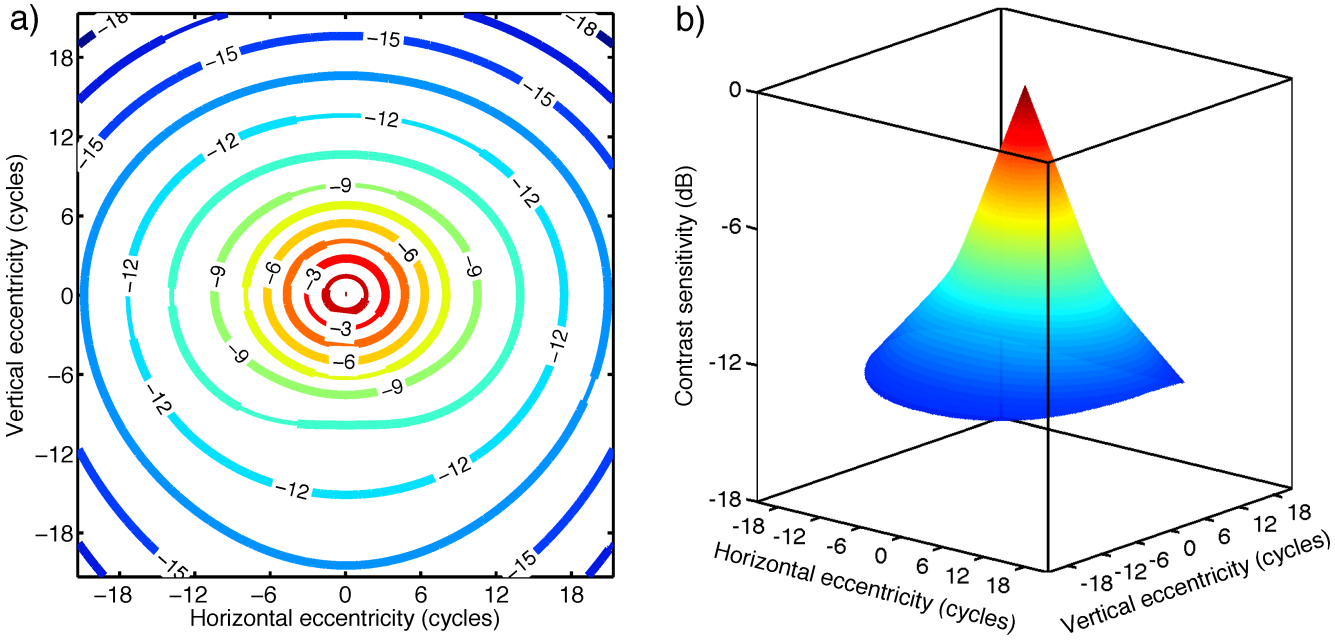

Figure 9. (a) A contour map (attenuation surface) of contrast sensitivity across the central visual field. The map is derived from the eight-parameter witch's hat (see Table 2) fitted to the averaged results of all four observers for vertical 4 c/deg stimuli (shown in Figure 5). (b) A surface plot showing the same attenuation surface. The shape of this surface prompted us to call it a witch's hat.

sensitivity from the signal to noise ratios of ideally-combined cone responses (as proposed by Ahumada & Watson, 2011) and found that the rate of decline was constant for different spatial frequencies when eccentricity was expressed in degrees of visual angle, not carrier cycles (see Appendix A). The basis by which the scale invariance of our result is derived remains unclear to us.

Orientation effects are either weak or absent in the central visual field

We found only marginal effects of orientation (either absolute or relative) suggesting that a good estimate of the attenuation surface within the central visual field can be achieved by gathering data for just a single target orientation. We also confirmed that a substantial relative orientation effect is found only at greater eccentricities than those concentrated on here.

Meridional anisotropies and constructing the witch's hat

The decline in contrast sensitivity was shallower along the horizontal meridians than the superior vertical meridians (cf. Pointer & Hess, 1989; Foley et al., 2007; Abrams et al., 2012). This effect was evident

	Model variant (column headings indicate the form of yoking)							
	v cy				v deg			
	m_1 cy		m_1 deg		m_1 cy		m_1 deg	
Parameter	m_2 cy	m_2 deg	m_2 cy	m_2 deg	m_2 cy	m_2 deg	m_2 cy	m_2 deg
ASB	0.740*	0.827	1.143	2.258	1.099	1.726	1.253	2.359
DHB	1.157	1.185	0.977	1.877	0.757*	2.142	1.007	1.938
SAW	0.679*	1.322	1.744	3.000	1.233	9.380	1.445	3.272
Average	0.594*	1.238	0.864	2.290	0.745	1.784	0.981	2.422

Table 5. RMS errors for 2 × 2 × 2 factorial model variants using each possible combination of the two methods of scaling the model parameters (by carrier cycles or visual angle). The model variants were fit to the family of spatial frequency functions collected from each of the three observers in Experiment 3 (Figure 6) and the average of those observers. When a parameter depended on carrier cycles no scaling was required, whereas when it depended on degrees of visual angle it was multiplied by the spatial frequency of the stimulus. Table entries are RMS errors (in dB) and an asterisk indicates the lowest error for each observer. The column headings indicate whether yoking was in cycles (cy) or degrees (deg). Typically, the RMS errors were lower when the parameters were yoked in cycles.

	Gradients (dB/cy)		Knee (cy)	k_2 per spatial frequency (c/deg)						RMSe
Observer	m_1	m_2	v	0.7	1	1.4	2	2.8	4	dB
ASB	1.14	0.40	7.94	−5.40	−3.50	−5.49	−4.89	−8.45	−9.66	0.740
DHB	0.97	0.55	9.85	−5.94	−6.30	−6.79	−9.18	−11.11	−14.16	1.157
SAW	2.15	0.63	4.64	−0.73	−1.27	−1.91	−6.21	−5.29	−9.90	0.679
AVERAGE	1.08	0.40	10.50	−4.61	−4.28	−5.32	−7.35	−8.87	−11.82	0.723

Table 6. Parameters for the witch's hat model fits in the left panels of Figure 6 and for a fit to the averaged data of the three observers.

in both limbs of the bilinear functions for all four observers confirming the horizontal–vertical anisotropy, though the effects were quite small (see Table 4). More striking was the finding that the second slope (m_2) of the inferior meridian was almost half that for the superior meridian, confirming the vertical-meridian anisotropy (Abrams et al., 2012). In fact, the second slope of the inferior meridian was even shallower than for the horizontal meridians.

Our success in using the results from the cardinal meridians to predict sensitivity for the diagonal meridians confirms Abrams et al.'s (2012) conclusion that the various benefits and inferiorities measured for different hemi-meridians vary smoothly with radial angle. It also shows that a good estimate of the attenuation surface can be achieved by judicious choice of sampling. For example, the different bilinear functions for the horizontal, superior, and inferior meridians suggest that the measurement of those three meridians is sufficient. Furthermore, because the curves for the different spatial frequencies are approximately vertical translations of each other when expressed in dB/cycle (Figures 6a, c, & e), this allows an attenuation surface derived from one spatial frequency to be generalized across other spatial frequencies when expressed in cycles of the carrier.

The witch's hat that we radially interpolated from the eight-parameter variant of the model outlined in the Descriptive modeling section is shown in Figure 9 (the details of the procedure are embedded in the Matlab code in Appendix B). These summarize our estimate of the spatial variation of contrast sensitivity across the central visual field. The general elliptical shape of this surface bears some similarity to a proposal by Pöppel and Harvey (1973), though it differs in its detail. For example, the shallow decline in sensitivity for the second limb in the inferior field tends to raise the brim of the hat at its front.

Summary and conclusions

The witch's hat description of the variation of binocular contrast sensitivity across the central visual field provides a more detailed account of the inhomogeneity than has previously been available. This is of value for any study involving detailed modeling of spatial pattern vision at contrast detection threshold in the central visual field, such as the results from Modelfest (Carney et al., 2000).

Acknowledgments

We thank Al Ahumada, Hans Strasburger, and an anonymous reviewer for their comments and suggestions. We also thank Rob Summers for help with the statistical analysis. This research was supported by the Engineering and Physical Sciences Research Council (EPSRC): grant number EP/H000038/1. Part of this work has appeared in abstract form at the 2010 AVA Spring Meeting (Baldwin, Meese, & Baker, 2010).

Commercial relationships: none.
Corresponding author: Alex S. Baldwin.
Email: alexsbaldwin@googlemail.com.
Address: School of Life & Health Sciences, Aston University, Birmingham, United Kingdom.

References

Abrams, J., Nizam, A., & Carrasco, M. (2012). Isoeccentric locations are not equivalent: the extent of the vertical meridian asymetry. *Vision Research*.

Ahumada, A. J., & Watson, A. B. (2011). Updating the standard spatial observer for contrast detection. *Investigative Ophthalmology & Visual Science, 52*: E-abstract 1879. [Abstract]

Akaike, H. (1974). A new look at the statistical model identification. *IEEE Transactions on Automatic Control*, *19*, 716–723.

Anderson, S. J., Mullen, K. T., & Hess, R. F. (1991). Human peripheral spatial resolution for achromatic and chromatic stimuli: Limits imposed by optical and retinal factors. *Journal of Physiology, 442*, 47–64.

Baker, D. H., & Meese, T. S. (2011). Contrast integration over area is extensive: a three stage model of spatial summation. *Journal of Vision, 11*(14):14, 1–16.

Baldwin, A. S., Meese, T. S., & Baker, D. H. (2010). Loss of contrast sensitivity at 4 cycles deg^{-1} depends on eccentricity and meridian but not grating orientation for the central 9 deg of the visual field. *Perception, 39*, 1151.

Berkley, M. A., Kitterle, F., & Watkins, D. W. (1975). Grating visibility as a function of orientation and retinal eccentricity. *Vision Research*, *15*(2), 239–244.

Campbell, F. W., Kulikowski, J. J., & Levinson, J. (1966). The effect of orientation on the visual resolution of gratings. *The Journal of Physiology, 187,* 427–436.

Carney, T., Tyler, C. W., Watson, A. B., Makous, W., Beutter, B., Chen, C.-C. et al. (2000). Modelfest: Year one results and plans for future years. In B. E. Rogowitz & T. N. Pappas (Eds.), *Proceedings of SPIE: Human Vision and Electronic Imaging V*, *3959*, 140–151.

Carrasco, M., Penpeci-Talgar, C., & Eckstein, M. (2000). Spatial covert attention increases contrast sensitivity across the CSF: Support for signal enhancement. *Vision Research*, *40*, 1203–1215.

Curcio, C., & Allen, K. (1990). Topography of ganglion cells in human retina. *The Journal of Comparative Neurology*, *300*, 5–25.

Curcio, C. A., Sloan, K. R., Kalina, R. E., & Hendrickson, A. E. (1990). Human photoreceptor topography. *The Journal of Comparative Neurology, 292*, 497–523.

Daniel, P. M., & Whitteridge, D. (1961). The representation of the visual field on the cerebral cortex in monkeys. *Journal of Physiology, 159*, 203–221.

Foley, J. M., Varadharajan, S., Koh, C. C., & Farias, M. C. Q. (2007). Detection of Gabor patterns of different sizes, shapes, phases and eccentricities. *Vision Research*, *47*, 85–107.

García-Pérez, M. A., & Peli, E. (2001). Luminance artifacts of cathode-ray tube displays for vision research. *Spatial Vision, 14*(2), 201–215.

Heeley, D. W., & Timney, B. (1988). Meridional anisotropies of orientation discrimination for sine wave gratings. *Vision Research, 28*(2), 337–344.

Hess, R. F., Baker, D. H., May, K. A., & Wang, J. (2008). On the decline of 1st and 2nd order sensitivity with eccentricity. *Journal of Vision, 8*(1):19, 1–12, http://www.journalofvision.org/content/8/1/19, doi:10.1167/8.1.19. [PubMed] [Article]

Hilz, R., & Cavonius, C. R. (1974). Functional organization of the peripheral retina: Sensitivity to periodic stimuli. *Vision Research, 14*(12), 1333–1337.

Johnston, A. (1987). Spatial scaling of central and peripheral contrast-sensitivity functions. *Journal of the Optical Society of America A*, *4*(8), 1583–1593.

Kelly, D. H. (1984). Retinal inhomogeneity. I. Spatiotemporal contrast sensitivity. *Journal of the Optical Society of America A, 1*(1), 107–113.

Koenderink, J. J., Bouman, M. A., Bueno de Mesquita, A. E., & Slappendel, S. (1978a). Perimetry of contrast detection thresholds of moving spatial sine wave patterns. I. The near peripheral visual field (eccentricity 0°–8°). *Journal of the Optical Society of America, 68*(6), 845–849.

Koenderink, J. J., Bouman, M. A., Bueno de Mesquita, A. E., & Slappendel, S. (1978b). Perimetry of contrast detection thresholds of moving spatial sine wave patterns. II. The far peripheral visual field (eccentricity 0°–50°). *Journal of the Optical Society of America, 68*(6), 850–854.

Koenderink, J. J., Bouman, M. A., Bueno de Mesquita, A. E., & Slappendel, S. (1978c). Perimetry of contrast detection thresholds of moving spatial sine wave patterns. III. The target as a sensitivity controlling parameter. *Journal of the Optical Society of America, 68*(6), 854–860.

Koenderink, J. J., Bouman, M. A., Bueno de Mesquita, A. E., & Slappendel, S. (1978d). Perimetry of contrast detection thresholds of moving spatial sine wave patterns. IV. The influence of mean retinal illuminance. *Journal of the Optical Society of America, 68*(6), 860–865.

Long, G. M., & Tuck, J. P. (1991). Comparison of contrast sensitivity functions across three orientations: Implications for theory and testing. *Perception*, *20*, 373–380.

Meese, T. S. (2010). Spatially extensive summation of contrast energy is revealed by contrast detection of micro-pattern textures. *Journal of Vision, 10*(8):14, 1–21, http://www.journalofvision.org/content/10/8/14, doi:10.1167/10.8.14. [PubMed] [Article]

Meese, T. S., & Summers, R. J. (2007). Area summation in human vision at and above detection threshold. *Proceedings of the Royal Society B: Biological Sciences, 274*, 2891–2900.

Meese, T. S., & Summers, R. J. (2012). Theory and data for area summation of contrast with and without uncertainty: Evidence for a noisy energy model. *Journal of Vision,* in press.

Michel, M., & Geisler, W. S. (2011). Intrinsic position uncertainty explains detection and localization performance in peripheral vision. *Journal of Vision, 11*(1):18, 1–17, http://www.journalofvision.org/content/11/1/18, doi:10.1167/11.1.18. [PubMed] [Article]

Peirce, J. W. (2007). The potential importance of saturating and supersaturating contrast response functions in visual cortex. *Journal of Vision, 7*(6):13,

1–10, http://www.journalofvision.org/content/7/6/13, doi:10.1167/7.6.13. [PubMed] [Article]

Pelli, D. G. (1985). Uncertainty explains many aspects of visual contrast detection and discrimination. *Journal of the Optical Society of America A, 2*, 1508–1532.

Perry, V. H., & Cowey, A. (1985). The ganglion cell and cone distributions in the monkey's retina: Implications for central magnification factors. *Vision Research*, *12*, 1795–1810.

Pointer, J. S., & Hess, R. F. (1989). The contrast sensitivity gradient across the human visual field with emphasis on the low spatial frequency range. *Vision Research*, *29*, 1133–1151.

Pöppel, E., & Harvey, L. O. (1973). Light-difference threshold and subjective brightness in the periphery of the visual field. *Psychologische Forschung, 36*(2), 145–161.

Rijsdijk, J. P., Kroon, J. N., & van der Wildt, G. J. (1980). Contrast sensitivity as a function of position on the retina. *Vision Research, 20*, 235–241.

Robson, J. G., & Graham, N. (1981). Probability summation and regional variation in contrast sensitivity across the visual field. *Vision Research*, *21*, 409–418.

Rovamo, J., Franssila, R., & Näsänen, R. (1992). Contrast sensitivity as a function of spatial frequency, viewing distance and eccentricity with and without spatial noise. *Vision Research*, *32*(4), 631–637.

Rovamo, J., Virsu, V., & Näsänen, R. (1978). Cortical magnification factor predicts the photopic contrast sensitivity of peripheral vision. *Nature, 271*, 54–56.

Rovamo, J., & Virsu, V. (1979). An estimation and application of the human cortical magnification factor. *Experimental Brain Research, 37*, 495–510.

Rovamo, J., Virsu, V., Laurinen, P., & Hyvarinen, L. (1982). Resolution of gratings oriented along and across meridians in peripheral vision. *Investigative Ophthalmology & Visual Science, 23*: 666–670, http://www.iovs.org/content/23/5/666. [PubMed] [Article]

Sasaki, Y., Rajimehr, R., Woo Kim, B., Ekstrom, L. B., Vanduffel, W., & Tootell, R. B. H. (2006). The radial bias: A different slant on visual orientation sensitivity in human and nonhuman primates. *Neuron, 51*, 661–670.

Strasburger, H., Rentschler, I., & Jüttner, M. (2011). Peripheral vision and pattern recognition: A review. *Journal of Vision, 11*(5):13, 1–82, http://www.journalofvision.org/content/11/5/13, doi:10.1167/11.5.13. [PubMed] [Article]

Virsu, V., & Rovamo, J. (1979). Visual resolution, contrast sensitivity, and the cortical magnification factor. *Experimental Brain Research, 37*, 475–494.

Wright, M. J., & Johnston, A. (1983). Spatiotemporal contrast sensitivity and the visual field locus. *Vision Research, 23*(10), 983–989.

Appendix A

Cone density fails to predict scale invariance

The cone density data of Curcio et al. (1990) were collapsed over four hemi-meridians and fitted by a 10th order polynomial to give density as a function of eccentricity (Figure A1). This one-dimensional function was extended to two dimensions (d) by treating it as a radial function. Following Anderson, Mullen, and Hess (1991), this was used to simulate a square cone matrix. (For ease of exposition we use the one-dimensional index i for the spatially two-dimensional functions in this appendix). A contrast attenuation factor (a) was calculated from the cone density (Ahumada & Watson, 2011; Anderson, Mullen, & Hess, 1991) as follows:

$$a_i = \sqrt{d_i}. \tag{A1}$$

This function was normalized to have a gain of unity at the origin (the central point of fixation).

The attenuation surface derived from the cone density function was incorporated into a model that combines responses from individual locations over space in order to predict the relative sensitivity to log-Gabor patches at different eccentricities (0 deg–12 deg of visual angle) and spatial frequencies (0.7–8.0 c/deg).

The predictions were calculated as follows. The signal (s) at each of n locations (i) was multiplied by the attenuation factor (a). Matching a template to the expected signal resulted in each of these terms being squared (see the numerator of Equation A2), after which they were scaled by the stimulus contrast (c). We assumed the signal at each location to be perturbed by independent Gaussian noise with unit standard deviation. Assuming an ideal observer, the noise is also weighted by the template. The standard deviation of the noise at each location was squared, and then those variances summed and the square root taken to find the standard deviation of the combined noise. Therefore, the signal-to-noise ratio (SNR) is given by:

$$SNR = \frac{\sum_{i=1}^{n}(cs_i^2a_i^2)}{\sqrt{\sum_{i=1}^{n}(s_i^2a_i^2)}}. \tag{A2}$$

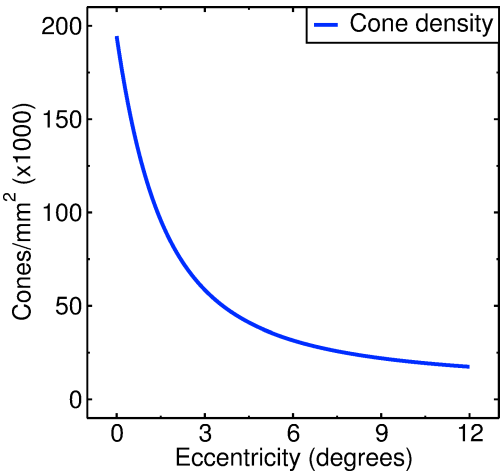

Figure A1. A one-dimensional polynomial fitted to the cone density data (not shown) from Curcio et al. (1990). A two-dimensional version was derived by treating this as a radial function. The two-dimensional version is the function d in our equations in this appendix.

Simplifying Equations A2 for a contrast of unity and substituting $\sqrt{d}$ for a gives the equation that we used to create the curves shown in Figure A2:

$$SNR = \sqrt{\sum_{i=1}^{n}(s_i^2 d_i)}. \quad \text{(A3)}$$

The curves in Figure A2 are close to parallel when eccentricity is expressed in degrees but diverge when it is expressed in stimulus carrier cycles. The prediction for the decline based on cone density shown here is most similar to our scale-invariant witch's hat result when the spatial frequency is around 2 c/deg (confirmed by a curve fitting procedure, not shown). This may account for why previous models that have used an attenuation surface based on cone density could provide acceptable fits for stimuli with spatial frequencies in that range (e.g., Ahumada & Watson, 2011). The lack of scale invariance shown here does not depend critically on our assumptions about how the signal and/or noise are combined over space. Different assumptions produced predictions with the same form as those here, but with slopes of uniformly steeper or shallower gradients.

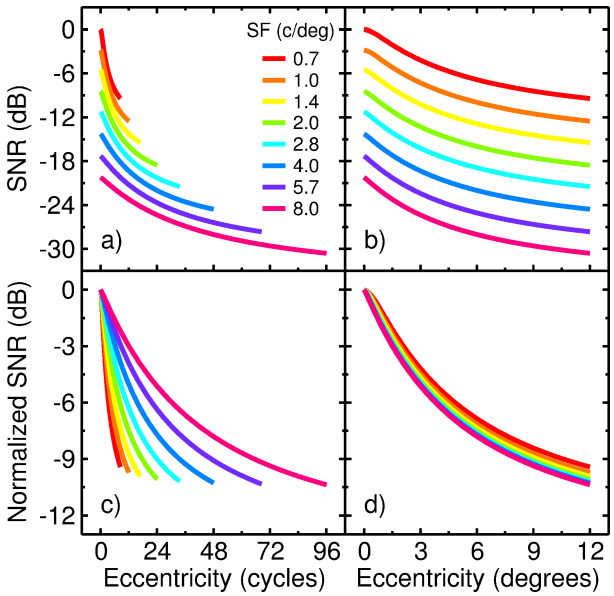

Figure A2. Contrast sensitivity predicted by the signal-to-noise ratios derived from the cone density data from Curcio et al. (1990) and Equation A3. Eccentricity is plotted as a function of carrier cycles and visual angle in the left and right columns respectively. Top: Each curve is normalized to the SNR for the 0.7 c/deg patch at an eccentricity of 0 deg. Bottom: Each curve is normalized to the SNR at an eccentricity of 0 deg for that spatial frequency.

Appendix B

Matlab code for the witch's hat

The Matlab code below produces a witch's hat attenuation surface from the eight-parameter fit, with the peak at 0 dB (k_2 is discarded).

```
function witchHat = witchhat(imSize,pixPerCycle,p)

% INPUT:    "imSize"      - the output image size
%           "pixPerCycle" - the wavelength of the spatial frequency
%           "p"           - a vector describing the bilinear falloff
%           [m1_sup m2_sup m1_inf m2_inf m1_hor m2_hor kneepoint]
% OUTPUT:   "witchHat"    - the witch hat attenuation surface

      % Convert input "p" to full 12-parameter witch's hat description
      x1dBL  = p(5);  x1dBR  = p(5); y1dBU  = p(1); y1dBD  = p(3);
      x2dBL  = p(6);  x2dBR  = p(6); y2dBU  = p(2); y2dBD  = p(4);
      kinkxL = p(7);  kinkxR = p(7); kinkyU = p(7); kinkyD = p(7);

      % Create variables holding position information
      x0 = ((imSize+1)/2); y0 = ((imSize+1)/2);
      [xx, yy] = meshgrid(1:imSize, 1:imSize);
      x1 = xx-x0; y1 = yy-y0;

      % Do geometry
      x1sq = real(x1.*x1); y1sq = real(y1.*y1);
      r = real(sqrt(x1sq + y1sq));
      ang = atan2(y1, x1);

      % Populate H&V meridian column vectors with parameters
      m1h   = x1dBL.*(x1<0)  + x1dBR.*(x1>0);
      m2h   = x2dBL.*(x1<0)  + x2dBR.*(x1>0);
      m1v   = y1dBU.*(y1>0)  + y1dBD.*(y1<0);
      m2v   = y2dBU.*(y1>0)  + y2dBD.*(y1<0);
      kneeh = kinkxL.*(x1<0) + kinkxR.*(x1>0);
      kneev = kinkyU.*(y1>0) + kinkyD.*(y1<0);

      % Interpolate between cardinal meridians using the equation for an ellipse
      % m1 & m2 (note that we must use the reciprocal of the gradient parameters)
      m1dB = (1./(m1h.*m1v))./(sqrt((cos(ang)./m1v).^2 + (sin(ang)./m1h).^2));
      m2dB = (1./(m2h.*m2v))./(sqrt((cos(ang)./m2v).^2 + (sin(ang)./m2h).^2));
      % kneepoint (note that we do not use the reciprocal of the knee parameter)
      knee = (kneeh.*kneev)./(sqrt((kneev.*cos(ang)).^2 + (kneeh.*sin(ang)).^2));

      % This is our standard bilinear equation, as a function of radial distance.
      % The three parameters (m1, m2 and the knee) vary with angle.
      % Note that we stored the gradient parameters (m1 and m2) as reciprocals,
      % so we must reciprocate again in this equation.

      k1 = log10(1 ./ (10 .^ ((1./m1dB - 1./m2dB) .* knee) + 1));

      surface = -log10( ...
                (10.^((1./m1dB) .* r./pixPerCycle)) ./         ...
                (10.^((1./m1dB - 1./m2dB) .* knee) +           ...
                (10.^((1./m1dB - 1./m2dB) .* r./pixPerCycle))) ...
                                                    ) + k1;
      witchHat = flipud(surface);

return
```